In situ studies on the kinetics of formation and crystal structure of $In_4Sn_3O_{12}$ using high-energy x-ray diffraction

G. B. González,[1,a)] J. S. Okasinski,[2] T. O. Mason,[3] T. Buslaps,[1] and V. Honkimäki[1]
[1]*Experiments Division, European Synchrotron Radiation Facility, F-38043 Grenoble, France*
[2]*Max-Planck-Institut für Metallforschung, D-70569 Stuttgart, Germany*
[3]*Department of Materials Science and Engineering, Northwestern University, Evanston, Illinois 60208, USA*

(Received 25 March 2008; accepted 19 June 2008; published online 25 August 2008)

High-energy x-ray diffraction was utilized to study *in situ* the formation temperature and crystal structure of the rhombohedral phase $In_4Sn_3O_{12}$. The kinetics of $In_4Sn_3O_{12}$ formation from bixbyite In_2O_3 and tetragonal SnO_2 nanopowders were investigated during isothermal annealing treatments ranging from 1335 to 1400 °C. The transformation data exhibited two regimes, well described with a two-exponent kinetics model. The first regime followed a Johnson–Mehl–Avrami–Kolmogorov (JMAK) behavior until 75% of the $In_4Sn_3O_{12}$ phase formed and was modeled with a modified JMAK equation. The formation of the first grains of $In_4Sn_3O_{12}$ at 1345 °C was observed *in situ* using diffraction two-dimensional images. Structural results obtained from Rietveld analysis include atomic positions, phase analysis compositions of the samples, and lattice parameters during heating, cooling, and isothermal conditions. Linear and volume coefficients of thermal expansion were determined for the $In_4Sn_3O_{12}$ phase. © *2008 American Institute of Physics*.
[DOI: 10.1063/1.2969913]

I. INTRODUCTION

At present, the most widely employed *n*-type transparent conducting oxides (TCOs) are based on tin oxide and Sn-doped indium oxide, also known as ITO. Due to their excellent electrical and optical properties, these TCOs are utilized in industrial applications that include flat-panel displays, solar cells, deicers, electrochromic windows, and mirrors.[1] These present and prospective applications have stimulated investigation into other similar TCOs that contain indium and tin, as well as other elements, such as zinc, cadmium, and gallium.[2–4] The lower indium content in $In_4Sn_3O_{12}$ compared to ITO results in a reduced material cost, making this phase a commercially promising TCO.

Tin oxide crystallizes in the rutile structure, space group $P4_2/mnm$, No. 136. The tetragonal lattice constants are $a=4.7374(1)$ Å and $c=3.1864(1)$ Å. There are two tin and four oxygen atoms per unit cell. Edge-sharing octahedrally coordinated tin ions form chains along the [001] direction.[5] From the oxygen perspective, tin atoms are located nearly at the corners of an equilateral triangle.

Both indium oxide and Sn-doped indium oxide exhibit the bixbyite structure. This fluorite-derived lattice, with space group $Ia3$, No. 206, has only three-fourths of the fluorite anion positions occupied by oxygen.[6] An In_2O_3 cubic cell of $a=10.117$ Å has a total of 80 atoms, 32 of which are cations occupying the 8*b* and 24*d* positions. Each cation lies at the center of a distorted cube with only six corners occupied by oxygen anions. The remaining two corners, located at the 16*c* positions, are empty and play an important role in the defect chemistry of Sn-doped indium oxide; i.e., they serve as available oxygen interstitial sites, which are partially occupied in ITO.[7]

Since 1985, several authors have reported the presence of an intermediate indium-tin oxide phase that forms at high temperatures and is closely related to bixbyite indium oxide.[8–14] All of these experiments were made on quenched samples prepared *ex situ*. These literature reports disagreed on the structure, stoichiometry, and temperature at which this fluorite-derived phase forms. Because the strongest peaks of this phase have similar *d* spacings to those of the bixbyite structure, it can be difficult to accurately index the phase and sometimes even to detect it in small concentrations. All reports agree that the formation temperature is higher than 1200 °C, and the more recent reports have observed it only at temperatures higher than 1300 °C.[9,12–14] Solov'eva and Zhdanov[8] indexed the phase as cubic pyrochlore $In_2Sn_2O_{7-x}$ ($a=10.226$ Å). Enoki and Echigoya[10] also described the phase as cubic with a lattice parameter of $a=10.21$ Å but did not report its stoichiometry.

Bates *et al.*[9] indexed this oxide phase as a close-packed $M'_mM''_nO_{3m}$ compound with rhombohedral structure due to its similarity with Tb_7O_{12} and Pr_7O_{12}. They observed this phase at 1552 °C and determined the lattice parameters to be $a=9.4810$ Å and $c=8.8452$ Å at 40% mol In_2O_3 and 60 mol % SnO_2. They found that with increasing In_2O_3, the *c* parameter almost doubled to 17.709 Å. Enoki *et a.*[11] indexed a hexagonal phase with lattice parameters of $a=9.5$ Å and $c=17.5$ Å. Ohya *et al.*[13] proposed that a hexagonal phase first appeared at 1380 °C. Heward and Swenson[14] observed the $In_4Sn_3O_{12}$ compound for temperatures ranging from 1350 to 1650 °C.

The most extensive study of the crystal structure of the high-temperature $In_4Sn_3O_{12}$ phase has been done by Nadaud

a)Present address: Department of Physics, DePaul University, Chicago, Illinois 60614, USA. Electronic mail: ggonza18@depaul.edu.

TABLE I. Samples prepared for this study. In_2O_3, SnO_2, and $In_4Sn_3O_{12}$ are expressed as weight percentages.

		Time at maximum temperature (h)		Initial atomic compositions		Final atomic compositions		
Sample No.	Temperature (°C)	Initial $In_4Sn_3O_{12}$ formation	Total	In_2O_3	SnO_2	$In_4Sn_3O_{12}$	ITO	SnO_2
1	1400	0.04	10	54.1(6)	45.9(4)	94.6(5)	2.7(2)	2.8(1)
2	1400	0.03	24	55.0(3)	45.0(5)	94.1(8)	5.2(5)	0.6(1)
3	1375	0.19	13	54.3(6)	45.7(4)	91.5(5)	4.3(2)	4.3(1)
4	1365	0.76	20	54.5(3)	45.5(4)	87.7(8)	7.3(4)	5.1(2)
5	1365	1.51	24	52.2(5)	47.8(3)	85.8(9)	4.3(6)	9.9(2)
6	1355	0.89	34	55.1(5)	44.9(4)	87.5(9)	4.6(6)	7.9(2)
7	1345	4.39	32	52.2(5)	47.8(4)	49.5(8)	27.0(8)	23.5(3)
8	1335	No formation	45	54.5(7)	45.5(5)	0	56.4(9)	43.6(5)

et al.[12] They formed the phase at 1550 °C and collected neutron diffraction data on quenched samples. The phase was indexed as hexagonal, belonging to space group $R\bar{3}$ and with lattice parameters $a=9.4602(2)$ Å and $c=8.8584(2)$ Å. Similar to the bixbyite structure, the model for this fluorite-derived phase has two nonequivalent cation sites, lattice oxygen anions, and space for interstitial oxygen anions. The 21 cations are located in the 3*a* and 18*f* sites, while the 36 lattice oxygen anions are found in the 18*f* sites.

Brilliant, high-energy x-ray radiation, produced from third-generation synchrotron sources, is an attractive tool for high-temperature *in situ* studies due to its large penetration length and small diffraction angles. When using a two-dimensional detector to collect diffracted data, entire Debye rings can be measured in a timeframe of seconds. Also, the appearance of phases, even low concentrations, can be detected more easily. The resolution of the diffraction data can be selected to separate peaks of closely matched *d* spacings by using a small beam size on the order of a hundred microns and by adjusting the sample-to-detector distance. The combination of all of these features enables the use of small temperature-stable furnaces to heat samples and simultaneously measure diffraction patterns with short exposure times.

The aim of the present work was to study *in situ* the kinetics of formation and structure of the high-temperature phase using high-energy x rays and an area detector. To vary the overall composition, different combinations of nano-In_2O_3 and nano-SnO_2 powders were used as starting materials. The crystal structure and phase fractions of all phases present were determined using Rietveld analysis from room temperature up to 1400 °C and back down to room temperature. Additionally, the indium and tin compositions of the samples were independently measured with x-ray fluorescene (XRF) analysis to corroborate the stoichiometry of the transformed phase.

II. EXPERIMENT

A. Sample preparation

Nano-In_2O_3 99.999% and nano-SnO_2 99.995+% powders (Aldrich Chemical Co., Milwaukee, WI, USA) were combined to obtain homogenous mixtures. The starting SnO_2 and In_2O_3 compositions are found in Table I. The powder mixtures were homogenized with acetone in a mortar and pestle and pressed into pellets 5 mm in diameter and 1 mm thick. The density of the pellets was approximately 50% the theoretical value. The grain size of the starting materials was on the order of 20 nm, as determined by both scanning electron microscopy (SEM) and x-ray diffraction (XRD) experiments.

B. Synchrotron x-ray powder diffraction experiments

High-energy x-ray experiments were performed at the ID15B beamline of the European Synchrotron Radiation Facility (ESRF). Because high-energy radiation can penetrate deep into materials, the diffraction data collected in transmission mode are representative of the bulk sample.

A Si 511 cylindrically bent Laue crystal monochromatized the x-ray radiation to an energy of approximately 90 keV. The exact x-ray energy was calibrated during each experiment with either Si or the LaB_6 NIST standard reference material 660a. A small incident beam of 200×200 μm^2 was used to diffract from the pellet samples. Debye rings were collected in the forward direction using a two-dimensional MAR345 image plate with a diameter of 345 mm and a 2300×2300 pixel array. The sample-to-detector distance was chosen to be approximately 1300 mm to obtain well-resolved peaks. The exact distance was determined for each sample independently. The instrumental resolution was determined from the diffraction pattern of the LaB_6 NIST standard reference powder 660a.

The samples were heated inside of a furnace, constructed from an inner alumina cylinder wrapped with a Pt/Rh heating element and surrounded by a water-cooled stainless steel jacket. A thermocouple inside the furnace provided feedback for temperature control. Two small windows with 1.3 and 13 mm in diameters let the incident and diffracted beams, respectively, pass through the furnace while minimizing thermal gradients. Under these experimental conditions, reflections up to *d* spacings of approximately 1 Å could be collected.

In order to obtain an accurate measurement of the temperature, a type *S* thermocouple was mounted in contact with the edge of the sample. The thermocouple readings were measured with a temperature controller (Eurotherm 2408i) and recorded at the same time the diffraction data were being collected. The heating and cooling rates of the furnace were 5 °C/min. Numerous samples with different maximum heat-

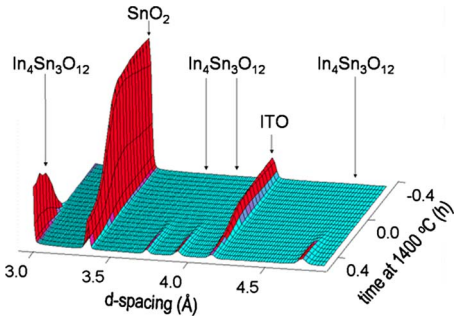

FIG. 1. (Color online) Evolution of ITO, SnO_2, and $In_4Sn_3O_{12}$ phases up to 1400 °C. For times less than zero, the sample temperature is increasing at a rate of 300°/h. At time equals zero, the temperature reaches 1400 °C and is subsequently held constant.

ing temperatures were used to determine the formation temperature and to study the isothermal kinetics of formation. The maximum temperatures of heating ranged from 1335 up to 1400 °C. The holding times at the maximum temperature ranged from 10 to 45 h.

The two-dimensional image collection time was 130 seconds, of which the exposure to the diffracted x rays was 40 s. During the temperature ramp and the first hours after reaching the maximum temperature, diffraction images were taken under two alternating conditions: either the pellet was static or it was translating over a 0.4 mm range. The purpose of translating the pellet was to increase the number of grains sampled in order to obtain a better representation of the sample. The observation of the first few grains of the new forming phase was better achieved when the pellet was static. The translation of the pellet resulted in a temperature change of less than 1°. The two-dimensional images were integrated and geometrical corrections were applied using programs written in the software MATLAB (The MathWorks, Inc.). The resulting diffraction patterns were analyzed using the Rietveld method[15] with the program FULLPROF.[16]

The indium and tin concentrations for the pellets were determined with x-ray fluorescence (XRF) before and after the heating experiments. A Ge solid-state detector collected all the fluorescence lines from the sample using an incident x-ray energy of approximately 90 keV. The program X-FLU[17] was used to fit both the primary and secondary fluorescence lines in order to determine the indium and tin compositions.

III. RESULTS AND DISCUSSION

The eight samples prepared for this study are summarized in Table I. The Debye rings collected in the two-dimensional images were analyzed and integrated to obtain one-dimensional XRD patterns. Figure 1 shows a time-dependent section of the diffraction patterns during one experiment with a maximum temperature of 1400 °C. As the ITO and SnO_2 phases decrease, the $In_4Sn_3O_{12}$ phase appears immediately after the sample reaches 1400 °C. In this figure and throughout this report, times less than zero indicate that the sample is heating from room temperature up to its maximum temperature at a rate of 300°/h. At time equals zero, the maximum temperature is reached and is subsequently held constant for various periods of time, as listed in Table I.

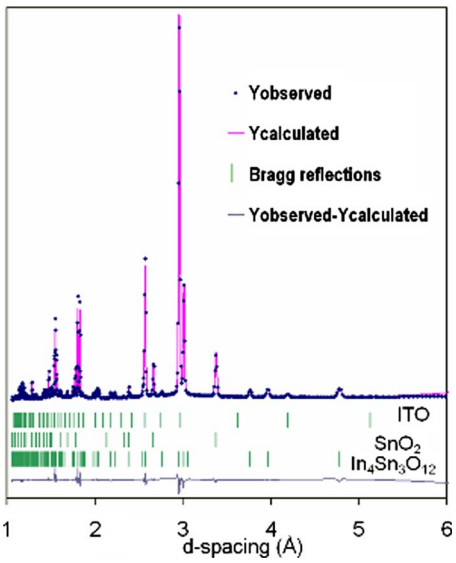

FIG. 2. (Color online) Rietveld refinement of x-ray synchrotron diffraction data on sample 6 after heating to 1355 °C for 18 h. Sample composition is 5.3(2)% ITO, 9.8(5)% SnO_2, and 84.9(5)% $In_4Sn_3O_{12}$.

The integrated XRD patterns were fitted with the Rietveld method. An example of a typical fitted pattern is illustrated in Figure 2, where Y (*observed*) and Y (*calculated*) correspond to the observed and calculated diffracted intensities. Y (observed)$-Y$ (calculated) represents the difference between the experimental and the modeled intensities, thus a zero difference curve corresponds to a horizontal line. The vertical bars indicate the positions of the Bragg reflections for each phase. In this figure, after an 18 h anneal at 1355 °C, this sample was triphasic with 5.3(2) wt % ITO, 9.8(5) wt % SnO_2, and 84.9(5) wt % $In_4Sn_3O_{12}$.

The formation temperature of $In_4Sn_3O_{12}$ occurred between 1335 and 1345 °C. Only the tetragonal and bixbyite phases were present in the sample heated at 1335 °C, even after annealing for 45 h. The hexagonal phase did form at 1345 °C, the next higher temperature studied. This observation disagrees with studies that report the phase at lower temperatures.[8,10,11,18] The temperature range for the formation of $In_4Sn_3O_{12}$ observed in the present experiment agrees with the phase diagram of Heward and Swenson,[14] where the formation temperature is reported between 1325 and 1350 °C. The fluorite-derived structures such as bixbyite and $In_4Sn_3O_{12}$ have diffraction patterns which are very similar, making their proper identification problematic at times. The small differences can be observed with high-quality diffraction data that combine highly resolved peaks and enough statistics, which may not have been easily available to the studies mentioned before.[8,10,11,18]

An isothermal transformation diagram for the temperatures investigated in this study is shown in Fig. 3, where the points correspond to the formation of the first grains of $In_4Sn_3O_{12}$ and at 25%, 50%, and 75% transformations. The kinetics of formation of the phase at 1345 °C were slow and after 800 min of annealing at this temperature, this phase constituted only 3 wt % of the sample. As mentioned previously, due to the close d-spacing matching of the strongest $In_4Sn_3O_{12}$ and bixbyite peaks in an x-ray pattern, the pres-

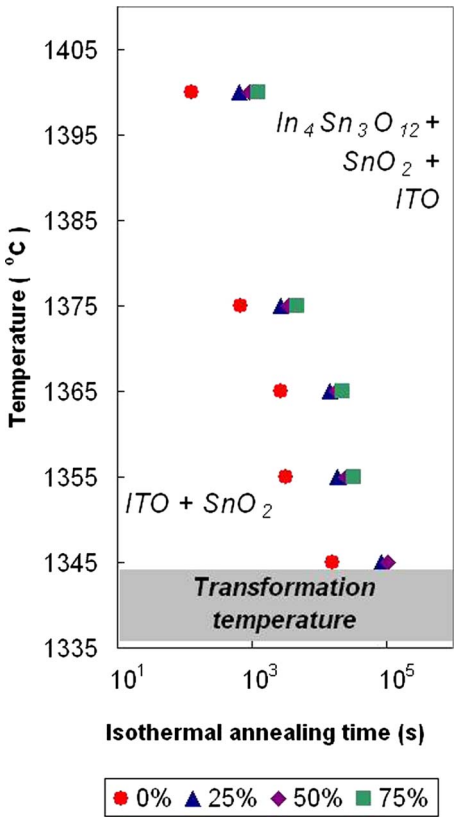

FIG. 3. (Color online) Isothermal diagram for the reaction $In_2O_3 + SnO_2 \Rightarrow In_4Sn_3O_{12} + ITO + SnO_2$.

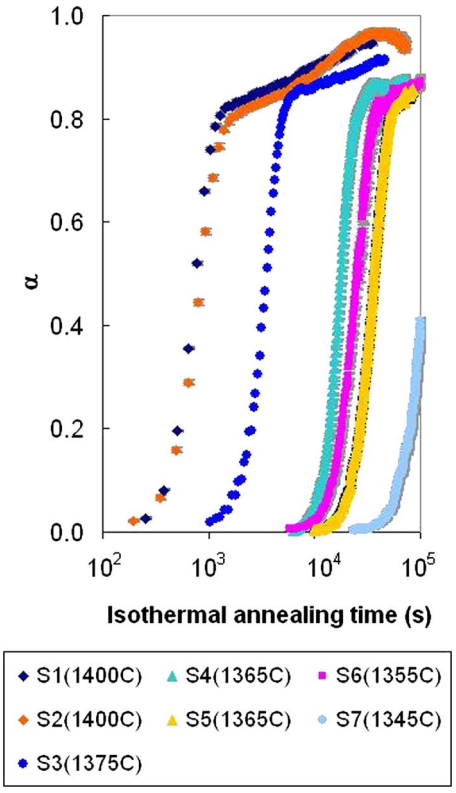

FIG. 4. (Color online) Kinetics of $In_4Sn_3O_{12}$ transformation for temperatures ranging from 1345 to 1400 °C.

ence of the phase is not readily apparent for concentrations lower than 1 wt %. A major advantage of using a two-dimensional detector when compared to a point counter is that the appearance of the new phase can be seen even when only a few grains are present. In this case, when the phase fraction is above one percent, the diffraction peaks from the integrated images start to become strong enough to be quantified reliably.

As expected, the kinetics of phase transformation become faster at higher temperatures, as seen in Fig. 4. At 1400 and 1365 °C two compositions were prepared. The samples that have an initial In_2O_3 and SnO_2 ratio with a stoichiometry closer to $In_4Sn_3O_{12}$ start forming the phase at an earlier time. Samples 2 and 4 form the rhombohedral phase before samples 1 and 5, respectively. The isothermal reaction kinetics of solid-solid phase transitions are usually expressed using the Johnson–Mehl–Avrami–Komolgorov (JMAK) equation,[19–23]

$$\alpha(t) = 1 - \exp\{-[k(T)t]^n\}, \tag{1}$$

$$\ln\{-\ln[1-\alpha(t)]\} = n\ln[k(T)] + n\ln(t), \tag{2}$$

where $\alpha(t)$ is the fraction of transformed $In_4Sn_3O_{12}$, t is the time, n is the Avrami exponent, and $k(T)$ is a temperature-dependent factor, sometimes called thermally activated rate constant. If the Avrami model is followed, for a given temperature, the slope n should be constant throughout time. As shown in Fig. 5, the behavior of the kinetics observed for this experiment is different since n changes with time as the reaction progresses. At early times of transformation the slope is constant up to approximately 75% of transformation. Beyond this point the slope decreases abruptly at all temperatures studied.

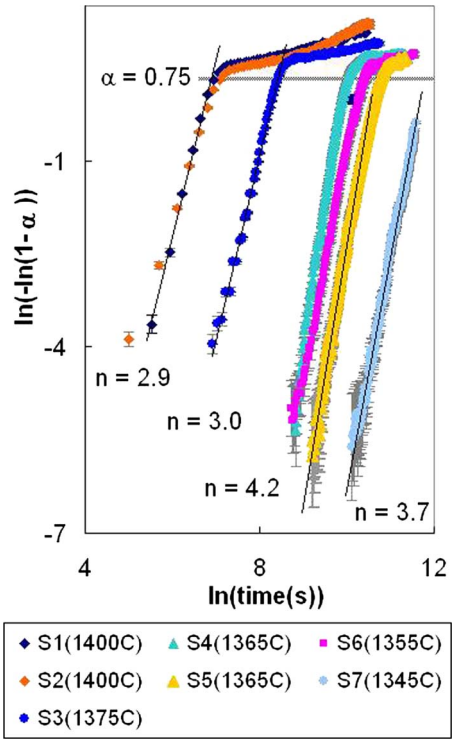

FIG. 5. (Color online) Isothermal kinetics of $In_4Sn_3O_{12}$ formation according to the Avrami equation. The Avrami exponents, obtained from the slopes, are fitted only in the linear range up to $\alpha \sim 0.75$.

TABLE II. Kinetics parameters obtained from fitting Eq. (3) to the $In_4Sn_3O_{12}$ transformed fraction. Only early and intermediate times of transformation are modeled.

Parameter	Sample 1	Sample 2	Sample 3	Sample 4	Sample 5	Sample 6	Sample 7	
$k(\times 10^{-5})$	128.4(3)	113.7(5)	27.161(3)	5.373(3)	2.638(2)	3.769(4)	0.8731(1)	
n	3.02(2)	2.62(3)	3.42(1)	4.34(1)	3.77(1)	3.55(1)	3.65(1)	
SF	0.829(1)	0.820(2)	0.853(1)	0.8617(5)	0.8372(6)	0.8604(4)	0.85	(fixed)
R^2	0.9997	0.9996	0.9996	0.9993	0.9996	0.9992	0.9958	

The Avrami exponent is a function of nucleation and growth parameters. It reaches its maximum value when a steady state nucleation rate is obtained.[24] At later times, the nucleation rate decreases, most likely due to increasing saturation of nuclei in the microstructure. The nucleation rate eventually approaches zero when complete saturation occurs. This leads to an overall reduction in n. From then on, the transformation rate is mostly controlled by growth rather than nucleation.[24,25] The Avrami exponents are interpreted in the literature as parameters indicating the dimensionality of the growth and the mode of transformation. The values of n in the present experiment range from 3 to 4 if only the linear part of the curves is considered ($0<\alpha<0.75$). Smaller n values are obtained for higher temperatures indicating that the nucleation and growth mechanisms may change with temperature. An n value of three corresponds to a mechanism where all particles grow in three dimensions starting from small size.[26] As summarized by Cumbrera and Sánchez-Bajo,[27] at zero nucleation rate, where saturation of point sites occurs, n equals 3. With a decreasing nucleation rate, n can range from 3 to 4, and at a constant nucleation rate, n is 4. For diffusion-controlled reactions, values of n less than 1 correspond to processes where particles have only modest grain growth.[26,27] Therefore, the small n values at late stages of transformation (after $\alpha>75\%$) might indicate that the kinetics are dominated by the slow growth of large particles.

The JMAK model is valid under specific conditions, summarized by Starink.[28] The initial sample composition must be homogeneous, and the nucleation sites and phases form with a random distribution. The average growth rates must be the same throughout the sample. Time-dependent processes, which are not directly related to the transformation, should not affect the reaction. Impingement and blocking caused by anisotropic growth should be negligible. The equilibrium state is constant so that the transformation is time independent. Numerous cases are reported in the literature where the JMAK equation is not followed because the previous conditions are not met.[24–31]

Kinetic models, such as that of Starink[28] and Austin and Rickett,[30] were also considered. These take into account impingement of growing particles. However, the improvements over the JMAK model were marginal at best, and similar deviations after 75% $In_4Sn_3O_{12}$ transformation rates were observed. Applying a scaling factor (SF) correction to the JMAK model, as shown in Eq. (3), significantly improved the fitting,

$$\alpha(t) = \mathrm{SF}\{1 - \exp(-[k(T)t]^n)\}. \tag{3}$$

The fitted parameters are found in Table II when data at early and intermediate stages of transformation were modeled. Figure 6 illustrates the model with a scaling factor compensating for the slowing of the kinetics immediately after 75% transformation rate is achieved. However, for longer annealing times and transformation fractions greater than 75%, JMAK-like equations do not fit appropriately the present experimental data since two kinetics regions exist. The full transformation curves for samples 1–3 can be well described using a model with two kinetic regimes similar to that by Bab *et al.*,[31]

$$\alpha(t) = \alpha_{\mathrm{sat}}\left\{\frac{[k(T)t]^{m_1}}{1+[k(T)t]^{m_2}}\right\}, \tag{4}$$

where α_{sat} is a scale factor, m_1 and m_2 are two exponents, $k(T)$ is again a temperature-dependent factor, t is the time, and α is transformed fraction of $In_4Sn_3O_{12}$. Table III shows

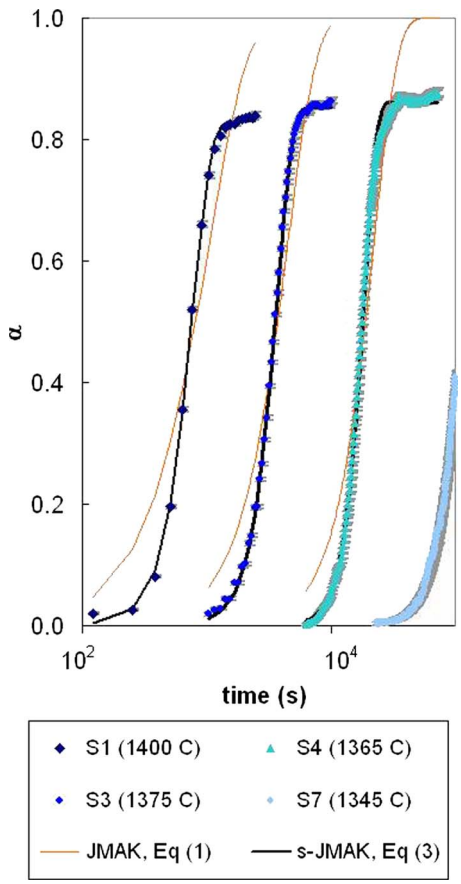

FIG. 6. (Color online) Model fits to the transformed fraction of $In_4Sn_3O_{12}$ for samples 1, 3, 4, and 7 using Eqs. (1) and (3). Early and intermediate stages of transformation are fitted.

TABLE III. Kinetics parameters obtained from fitting Eq. (4) to the transformed $In_4Sn_3O_{12}$ fraction in samples 1–3. The fitted data cover all measured times until the $In_4Sn_3O_{12}$ phase fraction approaches 1.

Parameter	Sample 1	Sample 2	Sample 3
$k(\times 10^{-4})$	15.24(4)	13.94(5)	3.111(3)
m_1	4.30(3)	5.00(6)	5.01(2)
m_2	4.26(3)	4.94(6)	4.99(2)
α_{sat}	0.803(1)	0.755(2)	0.843(1)
R^2	0.999	0.997	0.998

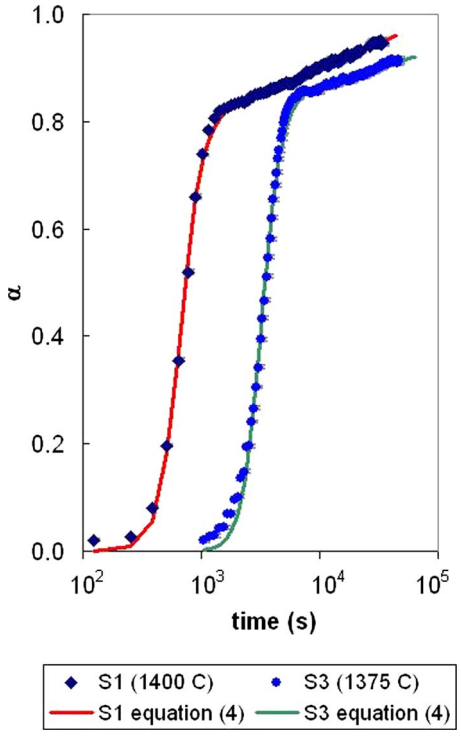

FIG. 7. (Color online) Model fits of Eq. (4) to the phase transformation data for samples 1 and 3. The fitted data cover all measured times until the $In_4Sn_3O_{12}$ phase fraction approaches 1.

the kinetics parameters obtained from Eq. (4), and Fig. 7 illustrates the modeled data for samples 1 and 3. The scale factor, α_{sat}, corresponds to the fraction where the kinetic mechanisms switch from nucleation controlled to growth controlled. As mentioned by Cumbrera and Sánchez-Bajo,[27] kinetic models with two exponential factors exhibit important similarities with the JMAK model. However, they have been used scarcely since the exponents have purely empirical significance. An estimate of the activation energy for the phase formation of $In_4Sn_3O_{12}$ is not reported here due to the limited temperature range that was studied.

The crystal structural parameters obtained for $In_4Sn_3O_{12}$ samples that were annealed at different temperatures are found in Table IV. The structure of $In_4Sn_3O_{12}$ is a rhombohedral distortion of the fluorite lattice, with space group $R\bar{3}$, as reported by Bates *et al.*[9] and Nadaud *et al.*[12] A total of 36 lattice oxygen anions are found in two different 18*f* general sites. The tin cations fully occupy the 3*a* sites and one third of an 18*f* general site position, while indium fills the remaining two-thirds of these general sites. Each cation in the higher symmetry 3*a* sites is found at the center of a cube where six of the eight corners contain oxygen anions at a distance of approximately 2.1(1) Å while the remaining two corners are empty. On the other hand, each cation in the 18*f* sites is located at the center of a distorted cube where only one corner is empty and seven are occupied with oxygen anions at different distances: 1.9(2), 2.0(1), 2.1(1), 2.2(2), 2.3(2), 2.5(1), and 2.8(2) Å. The values for the atomic positions at elevated temperatures in Table IV are very close to those determined by Nadaud *et al.*[12] at room temperature. The crystal structure of $In_4Sn_3O_{12}$ was retained and the atomic positions did not change significantly as the samples cooled from high temperatures at a rate of 300 °C/h. The doubling of the *c* lattice parameter of $In_4Sn_3O_{14}$, as reported by Bates *et al.*[9] and Enoki and Echigoya,[10] was not observed

TABLE IV. Rietveld refinement results for the phase $In_4Sn_3O_{12}$ (space group $R\bar{3}$) from 1345 °C to 1400 °C.

		Sample 1	Sample 2	Sample 3	Sample 4	Sample 5	Sample 6	Sample 7
Maximum T(°C)		1400	1400	1375	1365	1365	1355	1345
Annealing time (hr)		10	24	13	20	24	34	32
Maximum $In_4Sn_3O_{12}$(%)		94.6(5)	96.7(7)	91.5(5)	87.7(8)	85.8(9)	88.6(9)	49.5(8)
Cation 1	$x=y=z$	0	0	0	0	0	0	0
Cation 2	x	0.2525(2)	0.2524(3)	0.2527(2)	0.2524(3)	0.2520(4)	0.2522(3)	0.2519(4)
	y	0.2133(2)	0.2125(2)	0.2135(2)	0.2130(3)	0.2126(4)	0.2138(3)	0.2139(4)
	z	0.3457(2)	0.3465(3)	0.3458(2)	0.3469(3)	0.3458(4)	0.3455(3)	0.3452(5)
Oxygen 1	x	0.189(2)	0.190(2)	0.192(1)	0.196(2)	0.197(3)	0.204(2)	0.207(3)
	y	0.185(2)	0.184(3)	0.186(2)	0.184(3)	0.175(5)	0.171(3)	0.191(4)
	z	0.120(1)	0.127(1)	0.121(1)	0.146(2)	0.108(2)	0.099(1)	0.129(2)
Oxygen 2	x	0.199(2)	0.193(2)	0.198(2)	0.186(3)	0.188(4)	0.192(3)	0.188(4)
	y	0.992(2)	0.986(2)	0.994(2)	0.983(3)	0.973(4)	0.985(3)	0.999(4)
	z	0.385(1)	0.394(1)	0.392(1)	0.407(1)	0.390(2)	0.373(1)	0.392(2)
Rietveld	R_{Bragg}(%)	3.7	4.7	4.7	5.1	6.9	5.3	5.3
parameters	R_{wp}(%)	4.0	4.0	3.9	5.4	5.7	5.2	4.3
	R_{exp}(%)	2.1	4.3	2.0	3.3	3.7	2.7	3.4
	R_p(%)	3.1	3.2	2.9	4.1	4.2	3.8	3.3
a	Å	9.5590(1)	9.5624(2)	9.5592(1)	9.5564(2)	9.5545(2)	9.5571(2)	9.5536(2)
c	Å	9.0370(1)	9.0400(2)	9.0362(1)	9.0324(2)	9.0283(2)	9.0320(2)	9.0293(2)

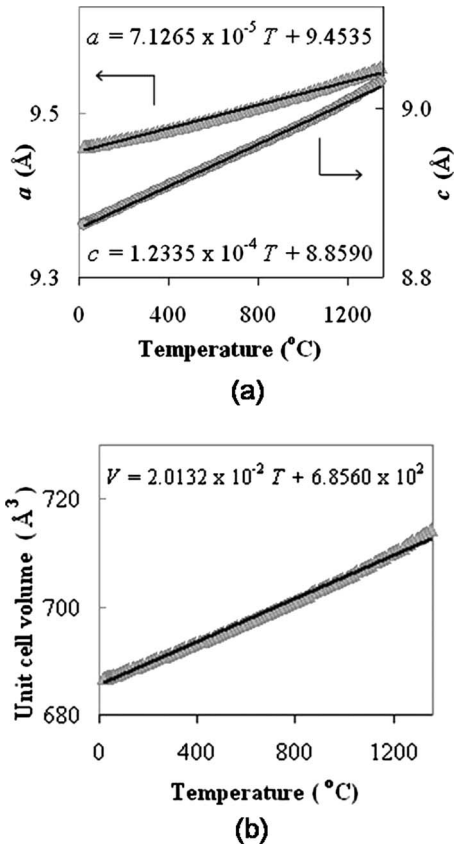

FIG. 8. Unit cell parameter changes in $In_4Sn_3O_{12}$ during a cooling experiment from 1355 °C to room temperature. (a) Linear contraction of the *a* and *c* lattice parameters. (b) Volume contraction.

in the present study. Past reports had also suggested the doubling of the *c* parameter in other isostructural M_7O_{12} phases, but this has not been replicated either.[32]

Linear and volume thermal parameters for the hexagonal phase were estimated from data collected during a cooling experiment. Figure 8(a) illustrates the contraction of the *a* and *c* parameters from 1355 °C to room temperature, while Fig. 8(b) shows the change in the unit cell volume. From the fitted linear functions in these figures, the thermal expansion coefficients were estimated as follows:

$$\alpha_a = \frac{\Delta a}{\Delta T a_0}, \tag{5}$$

$$\alpha_c = \frac{\Delta c}{\Delta T c_0}, \tag{6}$$

$$\beta = \frac{\Delta V}{\Delta T V_0}, \tag{7}$$

where a_0, c_0, and V_0 are the parameters at room temperature. The expansion coefficients are 7.538×10^{-6}/ °K for α_a and 1.392×10^{-5}/ °K for α_c. The volume coefficient β is equal to 2.936×10^{-5}/ °K. For ITO (data not shown), the thermal expansion coefficient α_a is 9.054×10^{-6}/ °K. These values assume that the material is polycrystalline and isotropic. SEM images show that the grains of the starting materials are approximately spherical before the temperature anneal.

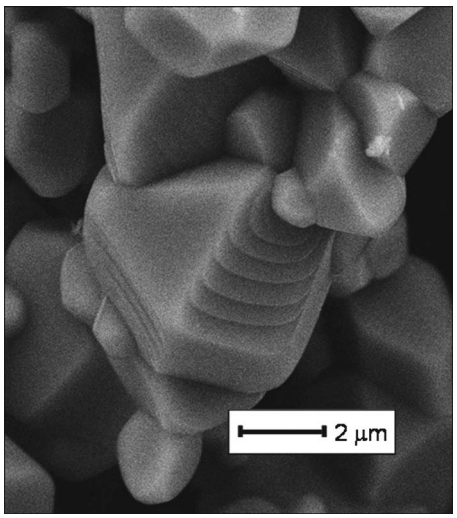

FIG. 9. SEM micrograph of sample 1 after 10 h of annealing at 1400 °C.

The initial particle size is on the order of 20 nm, in agreement with XRD results. The grains continue to grow in an isotropic manner until they reach micron sizes, when facets and terraces develop. Figure 9 shows the biggest grains observed in the sample annealed at the highest temperature. This image was taken after 10 h of annealing at 1400 °C.

Figure 10 shows the phases present during the annealing experiment in sample 2. The initial weight fractions remain constant until the sample reaches 900 °C. The slight decrease in SnO_2 and a corresponding increase in the bixbyite phase fraction above 900 °C are due to the formation of ITO. This observation is not surprising and confirms the results obtained in detailed studies of the In_2O_3–SnO_2 phase diagram.[14,33] The evaporation of tin becomes significant at higher temperatures and longer annealing times. At 1400 °C, the hexagonal phase formed in the first 2 min, and after 10 h, the hexagonal phase constituted 97 wt % of the sample. However, further annealing at this temperature decreased the fraction of $In_4Sn_3O_{12}$ phase while the fraction of ITO started

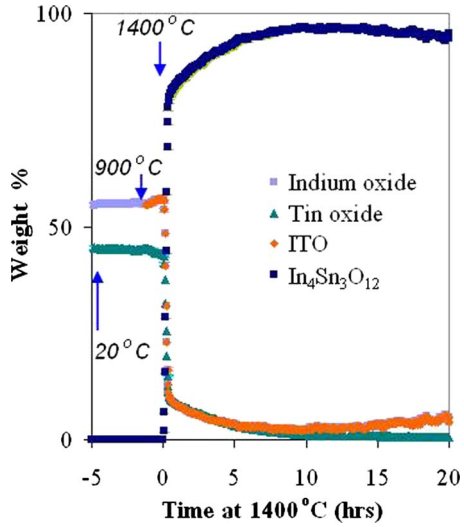

FIG. 10. (Color online) Composition of sample 2 during a heating experiment from room temperature up to 1400 °C, followed by a 20 h anneal at 1400 °C.

to increase. These observations indicate that tin evaporation is occurring because the SnO_2 phase does not reappear once it has been exhausted. Since $In_4Sn_3O_{12}$ has higher tin concentration than ITO, the evaporation of tin causes the decrease in $In_4Sn_3O_{12}$, and the remaining indium and oxygen recombine to form more of the bixbyite phase. The evaporation of tin in specimens annealed at high temperatures and long times was confirmed by XRF measurements collected before and after the annealing processes. Sample 2 suffered the biggest evaporation problem. After 24 h at 1400 °C, the tin loss in this sample was 3 cation % cation. Preferential evaporation of tin at high temperatures may result in the inference of incorrect phase stoichiometries in the absence of chemical composition analysis. The XRD and XRF results are consistent with the stoichiometry of $In_4Sn_3O_{12}$.

IV. CONCLUSIONS

High-energy XRD was used to study *in situ* the kinetics of phase transformation of SnO_2 and In_2O_3 mixtures under isothermal annealing conditions at temperatures from 1335 to 1400 °C. XRD and XRF results confirm that a rhombohedral phase with a stoichiometry of $In_4Sn_3O_{12}$ forms between 1335 and 1345 °C. The hexagonal phase did not decompose at lower temperatures, even during slow cooling from 1400 °C to room temperature. The kinetics of $In_4Sn_3O_{12}$ formation follow the JMAK model up to annealing times of 75% phase transformation. A modified JMAK model including a scaling factor improved the data fitting at early and intermediate transformation times. The deviation from JMAK-like models at later transformation times can be due to a heterogeneous distribution of nucleation sites in sample and to the slow kinetics of large particles growing. A model with two kinetic exponents and one thermally activated rate constant can well describe the behavior of the entire $In_4Sn_3O_{12}$ transformation up to times when nearly 100% phase transformation occurs.

ACKNOWLEDGMENTS

This work was performed at ID15B, the High-Energy Beamline of the European Synchrotron Radiation Facility (ESRF). The authors acknowledge Dr. Irina Snireva for her help with SEM images. T.O.M. acknowledges support from the NSF MRSEC program at Northwestern University under Grant No. DMR-0520513.

[1] R. G. Gordon, MRS Bull. **25**, 52 (2000).
[2] D. R. Kammler, B. J. Harder, N. W. Hrabe, N. M. McDonald, G. B. González, D. A. Penake, and T. O. Mason, J. Am. Ceram. Soc. **85**, 2345 (2002).
[3] A. Ambrosini, S. Malo, K. R. Peoppelmeier, M. A. Lane, C. R. Kannewurf, and T. O. Mason, Chem. Mater. **14**, 58 (2002).
[4] D. D. Edwards and T. O. Mason, J. Am. Ceram. Soc. **81**, 3285 (1998).
[5] A. A. Bolzan, C. Fong, B. J. Kennedy, and C. J. Howard, Acta Crystallogr., Sect. B: Struct. Sci. **53**, 373 (1997).
[6] M. Marezio, Acta Crystallogr. **20**, 723 (1966).
[7] G. B. González, T. O. Mason, J. P. Quintana, O. Warschkow, D. E. Ellis, J.-H. Hwang, J. P. Hodges, and J. D. Jorgensen, J. Appl. Phys. **96**, 3912 (2004).
[8] A. E. Solov'eva and V. A. Zhdanov, Inorg. Mater. **21**, 828 (1985).
[9] J. L. Bates, C. W. Griffin, D. D. Marchant, and J. E. Garnier, Am. Ceram. Soc. Bull. **65**, 673 (1986).
[10] H. Enoki and J. Echigoya, J. Mater. Sci. **26**, 4110 (1991).
[11] H. Enoki, J. Echigoya, and H. Suto, Phys. Status Solidi A **132**, K1 (1992).
[12] N. Nadaud, N. Lequeux, M. Nanot, J. Jové, and T. Roisnel, J. Solid State Chem. **135**, 140 (1998).
[13] Y. Ohya, T. ITO, M. Kaneko, T. Ban, and Y. Takahashi, J. Ceram. Soc. Jpn. **108**, 803 (2000).
[14] W. J. Heward and D. J. Swenson, J. Mater. Sci. **42**, 7135 (2007).
[15] H. M. Rietveld, Acta Crystallogr. **22**, 151 (1967).
[16] J. Rodríguez-Carvajal, An introduction to the program FULLPROF, Version 2001, Laboratoire Léon Brillouin, CEA-CNRS, Saclay, France.
[17] V. Honkimäki, K. Hämäläinen, and S. Manninen, X-Ray Spectrom. **25**, 215 (1996).
[18] T. Minami, Y. Takeda, S. Takata, and T. Kakumu, Thin Solid Films **308–309**, 13 (1997).
[19] M. Avrami, J. Chem. Phys. **7**, 1103 (1939).
[20] M. Avrami, J. Chem. Phys. **8**, 212 (1940).
[21] M. Avrami, J. Chem. Phys. **9**, 177 (1941).
[22] A. N. Kolmogorov, Izv. Akad. Nauk SSSR, Ser. Fiz. **3**, 355 (1937).
[23] W. A. Johnson and R. F. Mehl, Trans. Am. Inst. Min., Metall. Pet. Eng. **135**, 416 (1939).
[24] D. H. Bratland, Ø. Grong, H. Shercliff, O. R. Myhr, and S. Tjøtta, Acta Mater. **45**, 1 (1997).
[25] J. W. Cahn, Acta Metall. **4**, 449 (1956).
[26] M. J. Starink, J. Mater. Sci. **32**, 4061 (1997).
[27] F. L. Cumbrera and F. Sánchez-Bajo, Thermochim. Acta **266**, 315 (1995).
[28] M. J. Starink, J. Mater. Sci. **36**, 4433 (2001).
[29] E. R. Fotsing, H. Schmidt, G. Borchardt, C. Schmalzried, and R. Telle, Philos. Mag. **85**, 4409 (2005).
[30] J. B. Austin and R. L. Rickett, Trans. Am. Inst. Min., Metall. Pet. Eng. **135**, 396 (1939).
[31] M. A. Bab, L. A. Baum, and L. Mendoza-Zélis, Physica B (Amsterdam) **389**, 193 (2007).
[32] H. J. Rossell, J. Solid State Chem. **19**, 103 (1976).
[33] G. B. González, T. O. Mason, J. S. Okasinski, T. Buslaps, and V. Honkimäki (unpublished).